# Research on the Motion Characteristics of Microrobots in Complex Viscoelastic Fluid Environments

Feng Cao

School of Mechanical Engineering, Northwestern Polytechnical University, Xi'an 710072, China

cfeng09292212@163.com

**Abstract.** Microrobot technology demonstrates revolutionary potential in the biomedical field, enabling critical functions such as targeted drug delivery, minimally invasive interventions, and precise lesion clearance. However, significant challenges remain in understanding their motion mechanisms within complex biological environments. This study systematically investigates the dynamic behavior of capsule-shaped microrobots in Newtonian and viscoelastic fluids, focusing on the coupling effects of complex boundary conditions, surface-driven strategies, and rheological parameters. By constructing a multi-physics coupling framework based on the Linear Phan-Thien-Tanner (LPTT) constitutive model and employing numerical simulations and the control variable method, the nonlinear regulatory mechanisms of polymer viscosity $\mu_p$, relaxation time $\lambda$, and elongation rate $\varepsilon$ on motion performance are revealed.Key findings include:In Newtonian fluids, an exponential-type surface-driven velocity profile generates stable propulsion due to its high-gradient velocity distribution, resulting in significantly higher average speeds compared to logarithmic and sinusoidal profiles.In viscoelastic fluids described by LPTT, a critical threshold for polymer viscosity $\mu_p$ (0.005Pa·s) exists: below this threshold, elastic stress dominates propulsion, while above it, viscous dissipation reduces efficiency.The parameter relaxation time $\lambda$ regulates the dynamic balance between elastic stress accumulation and relaxation. Short $\lambda$ (e.g., in lymph) facilitates rapid response, whereas long $\lambda$ causes local stress concentration, hindering propulsion. The influence of elongation rate $\varepsilon$ is negligible in shear-dominated flow fields.The study proposes a multimodal driving strategy based on flow field-parameter adaptation criteria, providing theoretical guidance for targeted delivery and precise manipulation in heterogeneous biological environments such as blood and mucus. By integrating theory and simulation, this work lays a foundation for the design and optimization of next-generation medical microrobots.

**Keywords:** Microrobot; Complex boundary; Viscoelastic fluid; LPTT; Surface-driven strategy.

## 1. Introduction

Microrobot technology, as a frontier in modern biomedical engineering, is reshaping the boundaries of precision medicine. These micron-scale intelligent carriers exhibit transformative potential, achieving millimeter-level precision in vitro experiments [1,2] and making breakthroughs in targeted drug delivery [3,4], thrombus clearance [5,6], and toxin detection [7], among other biomedical applications [8–12]. However, in vivo applications present complex biological environments [13,14], where fluids such as saliva, blood, and mucus exhibit non-Newtonian properties [15]. Biological tissues display dynamic viscosity variations (0.1–10Pa·s), localized shear thinning (shear rates of 10–1000s^-1), and characteristic relaxation time differences (0.1–10s) [16,17], posing fundamental challenges to traditional Newtonian fluid-based models.

Current research on microrobots primarily focuses on motion mechanisms in simple geometric flow fields with flat or planar boundaries [18–20], while studies on complex boundary conditions (e.g., asymmetric, multiscale, or dynamically changing boundaries) remain limited [21,22]. Existing studies on non-Newtonian fluids often examine the isolated effects of single rheological parameters, leaving a gap in systematic analyses of multiparameter coupling effects. For instance, Ouyang et al. [23] compared microrobot performance in shear-thinning and shear-thickening fluids but did not explore the dynamic interplay between viscosity and elastic parameters. Similarly, Qin et al. [24] studied elastic filaments in shear-thinning fluids but did not quantify the coupling effects of elongation rate and shear-thinning indices.

Many studies [25–29] have developed theoretical models and numerical methods for multiparameter fluid dynamics, but practical applications in microrobot motion control require more realistic simulations and experiments. But, most current research [30–34] overlooks the dynamic responses of non-Newtonian fluids to shear rate, time (thixotropy), or temperature (e.g., body heat), leading to discrepancies between model predictions and real-world motion.

This study addresses these gaps by setting three surface velocity driving functions (exponential, logarithmic, sine) with the use of magnetic force, magnetic torque correction strategy to control the direction of motion and simulating complex geometric boundaries (e.g., gastric folds [35], intestinal villi [36]) using sinusoidal functions. Proposing a multi-physics coupling framework based on the LPTT constitutive model, validated for its accuracy in characterizing biological fluid dynamics [37–40]. Investigating the synergistic effects of $\mu_p$, $\lambda$, and $\varepsilon$ through controlled variable experiments.

The results reveal a flow field-parameter adaptation criterion: $\varepsilon$is negligible in shear-dominated flows but may dominate energy dissipation in extensional flows. These findings, combined with multimodal driving strategies [41], could advance solutions for 3D large-deformation fluid-structure interaction challenges [24].

## 2. Method

A 2D fluid domain and microrobot model were constructed (Figure 1). The capsule-shaped microrobot was modeled as a rigid material with density $\rho$. Dimensions are listed in Table 1.

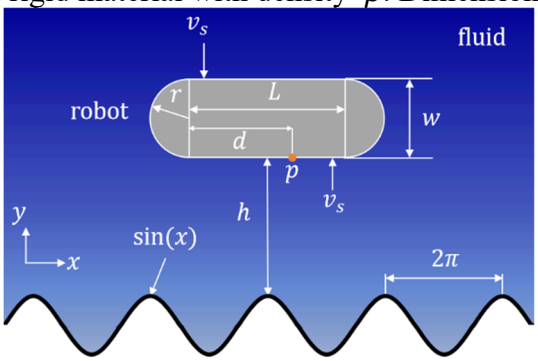


Figure 1 Model established for the simulation, indicating the size of the capsule-shaped miniature robot and the shape of its bottom edge

Table 1 Size parameters of the robot and the material density

| | |
|---|---|
| $L$ | 2μm |
| $w$ | 1μm |
| $r$ | 0.5μm |
| $\rho$ | 1000kg/m$^3$ |

The boundary shape and boundary conditions of the flow domain affect fluid flow characteristics such as velocity distribution and pressure distribution [42]. These fluid flow characteristics further influence the motion of micro-nano robots. For example, when approaching the boundary, micro-nano robots are affected by boundary-induced fluid flow, causing deflection of their motion trajectories or changes in velocity. This boundary effect is particularly pronounced in low-Reynolds-number flows [43]. To further investigate this mechanism, the shape of the bottom-wall boundary of the flow domain is set as a standard sine function curve, sin(x), in a two-dimensional flow domain plane coordinate system, with a period of 2πμmand an amplitude of 1μm.

As shown in (Figure 1), the distance between the bottom edge of the robot and the peak of the bottom-wall wave is set as h, which is a variable parameter. According to the existing studies by Wang [44], Gao [41], etc., the driving methods of miniature robots include magnetic-field driving, chemical driving, ultrasonic driving, etc. [14]. In this study, the surface-driving method is adopted, which can well simulate chemical driving and ultrasonic driving. The robot is assumed to have a wall velocity $\boldsymbol{v_s}$ in different forms. The magnitudes of the wall velocities on the upper and lower edges of the robot are the same, denoted as $\boldsymbol{v_s}$, but the distribution on the wall is non-uniform and is in the

form of a function. The variable $d$ of the function is defined as the distance from point p on the robot wall to the position shown in the figure.

In the research on the motion of squirmer in shear-thinning fluids [45], it is mentioned that: in Newtonian fluids, the $B_1$ mode (force dipole) obtained by Legendre decomposition of the flow-field velocity is the only mode that contributes to the swimming speed. Numerical simulations show that in non-Newtonian fluids, $B_1$ mode still dominates, but shear-thinning leads to a decrease in velocity. Higher-order modes (such as $B_3$ mode indirectly affect the velocity through the non-linear constitutive relation (local viscosity change coupled with the flow field), and may even reverse the trend (increase in velocity). Based on this, three functions are selected as the surface velocities in this study: the sine function, the natural exponential function, and the natural logarithmic function. Similar to the Legendre polynomial decomposition used in the study of squirmer, the driving velocity of the robot is Fourier-expanded, and it is considered that the magnitude of the velocity is mainly determined by the first-term sine function. To ensure that the magnitudes of the three velocity forms are consistent in the study, the sine function is taken as the reference, and the exponential function and the logarithmic function are divided by the coefficient of the first-term sine function in the Fourier expansion respectively to achieve this goal. Applying this conclusion in non-Newtonian fluids can be regarded as an innovation of this study.

Magnetic control enables the robot to achieve a higher motion speed, higher control precision, and realize flexible manipulation, etc. [1, 43]. To ensure that the robot moves steadily in one direction, an external gradient magnetic field $\boldsymbol{B}$ is required. By generating a magnetic force $\boldsymbol{F}$ and a magnetic torque $\boldsymbol{T}$, the stability of the motion trajectory is maintained at all times and the orientation of the robot is corrected. Assuming that the magnetic moment of the robot itself is $\boldsymbol{m}$, the generated magnetic force and magnetic torque are:

$$\begin{cases} \boldsymbol{F} = (\boldsymbol{m} \cdot \nabla)\boldsymbol{B} \\ \boldsymbol{T} = \boldsymbol{m} \times \boldsymbol{B} \end{cases}$$

First, in Newtonian fluids, the influence of the distance between the robot and the bottom-wall boundary on the average velocity $\bar{v}$ under three surface-velocity drivings is studied. Since the robot is rigid, the average velocity of any point on the robot is taken as the experimental result. The viscosity $\mu_s$ of Newtonian fluid is an important parameter, which describes the internal friction of the fluid. In Newtonian fluid research, the viscosity of the fluid is set as$1 \times 10^{-3}\mathrm{Pa} \cdot \mathrm{s}$ and the density $\rho_n$ is $1000\mathrm{kg/m^3}$. The continuity control equation indicates that the fluid is incompressible:

$$\nabla \cdot \boldsymbol{u} = 0$$

Table 2 Surface velocity patterns of robots. The first row is the set original function of the driving speed. The second row is the coefficient of the first sine function after the Fourier expansion of the original function. The third row is the actual driving speed after normalization by dividing the original function by the coefficient

| Original function | $\boldsymbol{sin}(\frac{\boldsymbol{d}}{\boldsymbol{L}}\boldsymbol{\pi})$ | $\boldsymbol{exp}(\frac{\boldsymbol{d}}{\boldsymbol{L}})$ | $\boldsymbol{ln}(\boldsymbol{1}+\frac{\boldsymbol{d}}{\boldsymbol{L}}\boldsymbol{\pi})$ |
|---|---|---|---|
| Coefficient of the first term | *1* | $\frac{4\pi(1-e)}{4\pi^2+1}$ | $\frac{-\pi}{ln2}$ |
| Surface velocity($\boldsymbol{\mu m}$/s) | $sin(\frac{d}{L}\pi)$ | $\frac{4\pi^2+1}{4\pi(1-e)}exp(\frac{d}{L})$ | $\frac{-ln2}{\pi}ln(1+\frac{d}{L}\pi)$ |

Meanwhile, the flow-field velocity cloud diagrams under three surface velocities at the initial moment in Newtonian fluid are given. They are measured on the same velocity scale, as shown in (Figure 2). These velocity distributions help understand the flow-field situation when the robot starts moving. The velocity distribution of the exponential function (exp) shows that the velocity increases rapidly from the center to the edge of the robot. This distribution may generate a large and uniform propelling force; thus, in (Figure 2), it shows the highest average velocity. The velocity distribution of the logarithmic function (ln) shows that the velocity increases gradually from the center to the edge. The propelling force generated by this distribution is moderate, resulting in an average velocity between that of the exponential function and the sine function. The velocity distribution of the sine

function (sin) shows periodic changes, with alternating high-speed and low-speed regions. This periodic velocity distribution may lead to fluctuations in the propelling force, and thus in (Figure 2), it shows the lowest average velocity. The initial velocity distribution is crucial for the robot's initial motion and the flow field's subsequent development. The velocity distribution of the exponential function, which is uniform and strong, may generate a more stable and efficient flow field, thereby increasing the velocity of the robot. The moderate velocity distribution of the logarithmic function leads to a moderate propelling force, while the periodic velocity distribution of the sine function may cause the flow field to be unstable, thus reducing the efficiency.

Then, the motion situation is studied in viscoelastic fluids. The governing equation for viscoelastic fluid motion is as follows:

$$\rho\frac{\partial \boldsymbol{u}}{\partial t}+\rho(\boldsymbol{u}\cdot\nabla)\boldsymbol{u}=\nabla\cdot[-p\boldsymbol{I}+\boldsymbol{K}+\boldsymbol{T_e}]+\boldsymbol{F}$$

where $u$ is the velocity field of the fluid, $p$ is the pressure, $\boldsymbol{I}$ is the unit tensor, $\boldsymbol{K}$ is the viscous stress tensor, $\boldsymbol{T_e}$ is the elastic stress tensor, and $\boldsymbol{F}$ is the external force. The expressions for $\boldsymbol{K}$ and $\boldsymbol{T_e}$ are as follows:

$$\boldsymbol{K}=\mu_s(\nabla\boldsymbol{u}+(\nabla\boldsymbol{u})^T)$$

$$\boldsymbol{T_e}=\sum_m \boldsymbol{T_{em}}$$

The elastic stress tensor is the sum of the elastic stress tensors of all modes.

Common constitutive models for viscoelastic fluids include Oldroyd-B, FENE-P, Giesekus, LPTT, etc. In this study, the LPTT constitutive model is chosen. The LPTT model is an improved viscoelastic fluid model that can more accurately describe the rheological properties of polymer solutions. This model takes into account the stretching and relaxation processes of polymer chains. Its constitutive equation is as follows:

$$\lambda\frac{\nabla}{\nabla t}\boldsymbol{T_{em}}+f_{rm}=2f_{pm}\mu_p S$$

where $\lambda$ is the relaxation time, and $f_{rm}$ and $f_{pm}$ are stress-related functions:

$$f_{rm}=\left[1+\frac{\lambda}{\mu_p}\varepsilon\mathrm{tr}(\boldsymbol{T_{em}})\right]\boldsymbol{T_{em}}, f_{pm}=1$$

Here,$\varepsilon$ is the elongation rate parameter of the fluid, and $\mu_p$ is the viscosity of the polymer solvent of the fluid.

$\frac{\nabla}{\nabla t}\boldsymbol{T_{em}}$ is the upper-convected derivative of the elastic tensor, and its expression is:

$$\frac{\nabla}{\nabla t}\boldsymbol{T_{em}}=\frac{\partial \boldsymbol{T_{em}}}{\partial t}+(\boldsymbol{u}\cdot\nabla)\boldsymbol{T_{em}}-\nabla\boldsymbol{u}\cdot\boldsymbol{T_{em}}-\boldsymbol{T_{em}}\cdot\nabla\boldsymbol{u}^T$$

The strain-rate tensor $\boldsymbol{S}$ is as follows:

$$\boldsymbol{S}=\frac{1}{2}(\nabla\boldsymbol{u}+\nabla\boldsymbol{u}^T)$$

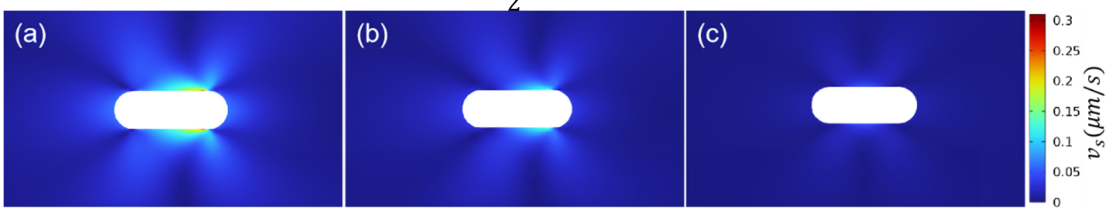


Figure 2. Flow-field velocity heatmaps under three driving velocities at the initial moment in Newtonian fluid. (a) Natural exponential function (exp), (b) Natural logarithmic function (ln), (c) Sine function (sin). They are represented on the same velocity-range scale

The LPTT model can better describe the shear-thinning and extensional viscosity characteristics of polymer solutions, and is suitable for describing the rheological behavior of polymer solutions under complex flow conditions [8]. This model has a high degree of accuracy in predicting the flow characteristics of polymer solutions. The three key variable parameters $\mu_p$, $\lambda$, $\varepsilon$ in its constitutive equation determine the viscoelasticity of the fluid, which are the focuses of this study. During the simulation process, the control variable method is used to study the effects of changes in these three parameters on the robot's motion speed respectively. Based on experience and relevant research,

reasonable ranges need to be determined for the three parameters to ensure the authenticity and rationality of the model. The initial values of $\mu_p$, $\lambda$, $\varepsilon$ are set as $1\times10^{-3}\mathrm{Pa}\cdot\mathrm{s}$, 0.01s, and 0.01 respectively, which are relatively close to the rheological characteristics of weakly viscoelastic polymer solutions such as respiratory mucus, gastrointestinal mucus, follicular fluid and other biological mucus. During the experiment, two of the variables are controlled at their initial values, and the effects of the changes of $\mu_p$in the range of $1\times10^{-3}-1\times10^{-2}\mathrm{Pa}\cdot\mathrm{s}$, $\lambda$ in the range of $0.01-0.1\mathrm{s}$, and $\varepsilon$ in the range of $0.01-0.1$on the robot's motion characteristics are studied respectively.

## 3. Results discussion

### 3.1 Results in Newtonian Fluids

In this set of simulation experiments, the distance h between the bottom edge of the robot and the peak of the sinusoidal-shaped boundary of the bottom wall of the flow domain is set to range from 2.5-8.5**μm**, with the lowest position being 2.5**μm**. For more details, see (Figure 1). Simulations are conducted at positions with an interval of 0.5**μm**. The simulation runs for 30s, and a typical motion effect is shown in the figure:

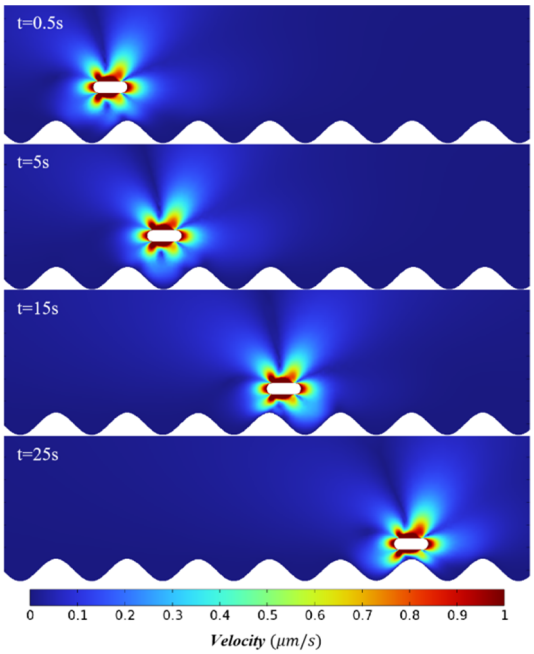


Figure 3. Snapshot of the robot's motion when the surface velocity is exp and the distance from the boundary is 2.5μm.

The average velocity during this period is calculated. (Figure 3) shows the relationship between $\bar{v}$ and $h$. The scatter plot is p lotted and fitted with a third-order polynomial to visually analyze the experimental results.

As the distance h increases, the average velocity of the miniature robot under the driving function shows a decreasing trend. The boundary-layer theory in fluid mechanics can explain this phenomenon. When the robot is close to the bottom wall, the fluid velocity gradient within the boundary layer is large, and the robot experiences a relatively large fluid resistance. However, due to the proximity to the boundary, the viscous effect of the fluid is strong, resulting in a relatively high velocity. As the robot moves away from the bottom wall, the boundary-layer effect weakens, and the fluid resistance increases, leading to a decrease in velocity.

The robot driven by the exponential function exhibits the highest average velocity for all values of h. For example, when $h$=2.5μm, the average velocity is1.098μm/s; even when $h$=8.5μm, the average velocity still remains at 0.927μm/s. Its fitting curve shows that the velocity gradually decreases as h increases, indicating that the exponential-function driving mechanism is stable and

efficient. The average velocity of the robot driven by the logarithmic function is between that of the exponential and sine functions. Its fitting curve shows that the velocity steadily decreases as h increases. The robot driven by the sine function shows the lowest average velocity for all values of h, which also decreases slightly as h increases, but with little overall change.

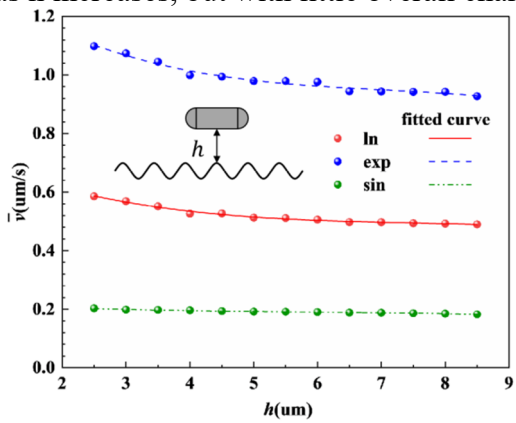


Figure 4 The simulation results of the robot at different distances from the bottom wall in Newtonian fluid. Blue (exp), red (ln), and green (sin) represent the results under three driving velocities respectively. The corresponding three curves are fitted curves.

Analyzing the results, the exponential function may generate a relatively strong propelling force in Newtonian fluid, enabling it to maintain a relatively high speed at different distances. The propelling force generated by the logarithmic function is more sensitive to the distance, resulting in a significant decrease in speed as $h$ increases. The periodicity of the sine function may lead to fluctuations in the propelling force, but has a relatively small impact on the overall speed, and its propulsion efficiency is always low.

In addition, the sinusoidal-shaped boundary of the bottom wall also has a certain impact on the robot's motion speed. The sinusoidal-shaped boundary increases the complexity of fluid flow, and the flow-field distribution shows periodic changes. There are differences in the fluid velocity and pressure distribution in the peak and trough regions, affecting the force acting on the robot at different positions. When the robot is close to the peak, it may be subject to stronger fluid resistance or propelling force, depending on the flow-field distribution and the characteristics of the robot's surface velocity. The interaction between the flow-field changes caused by this boundary shape and the robot's surface velocity distribution further affects the robot's average velocity. For example, when the robot driven by the exponential function is close to the peak, its high-gradient velocity distribution may interact with the local flow field to generate a stronger propelling force, thus offsetting the speed decrease caused by the boundary-layer effect to a certain extent. Due to the periodic fluctuations in its velocity distribution, the robot driven by the sine function may have more coupling effects with the flow-field changes caused by the sinusoidal-shaped boundary, resulting in a large difference in its propulsion efficiency at different positions.

### 3.2 Research Results on $\mu_p$ in Viscoelastic Fluids with the LPTT Constitutive Model

The research is carried out within the LPTT model set as described above. Using the control-variable method,$\lambda$ and $\varepsilon$ are kept unchanged at 0.01 s and 0.01 respectively, while $\mu_p$ is varied within the range of $0.001 - 0.01$Pa·s. (Figure 4) shows the relationship between $\bar{v}$ and $\mu_p$.

As can be seen from the figure, under the exponential-function driving, $\bar{v}$ increases from $0.215\mu m/s$ when $\mu_p = 0.001$ Pa·s to a peak value of $0.256\mu m/s$ when $\mu_p = 0.01$ Pa·s, indicating the existence of a critical threshold for the viscoelastic response. Subsequently, it decreases to $0.214\mu m/s$when $\mu_p = 0.01$Pa·s, showing a significant non-monotonic parabolic shape. This phenomenon can be explained by the competitive mechanism between the elastic stress tensor $\boldsymbol{T_e}$ and the viscous stress $\mu_p \nabla \boldsymbol{u}$ in the LPTT constitutive equation [40, 46]. In the low $\mu_p$ region ($\mu_p < 0.005$Pa · s), the polymer viscosity is low, and the elastic stress $\boldsymbol{T_e}$dominates. The high-gradient

velocity distribution of exponential driving (the edge velocity is significantly higher than the center) can stimulate a significant stretching component of the strain rate $\boldsymbol{S}$ under low stress $\mu_p$, thereby increasing the reaction force of the fluid on the robot and improving the propulsion efficiency. In the high-$\mu_p$ region ($\mu_p > 0.005\text{Pa}\cdot\text{s}$), as $\mu_p$ increases, the contribution of the viscous stress$\mu_p\nabla\boldsymbol{u}$ strengthens, resulting in rapid energy loss through viscous dissipation ($\propto \mu_p|\nabla\boldsymbol{u}|^2$). At the same time, the shear-thinning effect in the LPTT model is suppressed (an increase in $\mu_p$ reduces shear sensitivity), further weakening the dynamic response ability of the elastic stress, and ultimately leading to a decrease in velocity.

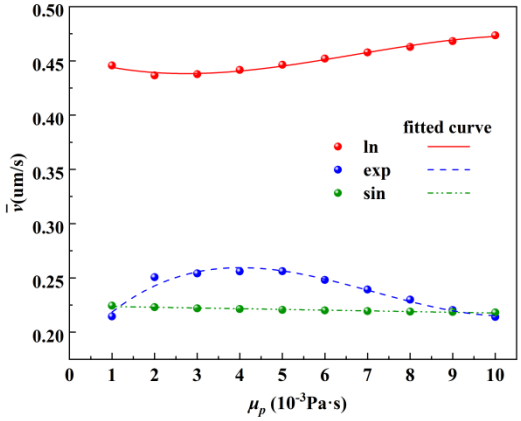


Figure 5 The results of average velocity $\bar{v}$ obtained from simulations where $\mu_p$ varies in the range of 0.001-0.01Pa · s in the viscoelastic fluid of the LPTT constitutive model, with $\lambda$ and $\varepsilon$ kept constant at 0.01s and 0.01 respectively, The blue (exp), red (ln), and green (sin) represent the results under three driving velocities respectively. The corresponding three curves are fitting curves.

In viscoelastic fluids, the $\bar{v}$ generated by exponential-function driving drops to around 0.2μm/s, much lower than the situation in Newtonian fluids. This phenomenon can be attributed to the characteristics of viscoelastic fluids and the complex interaction between the velocity distribution of exponential-function driving and the internal stress of the fluid. In Newtonian fluids, the fluid viscosity is constant and the flow behavior is relatively simple. However, in viscoelastic fluids, parameters such as polymer viscosity, relaxation time, and elongation rate are coupled with each other, making the fluid flow behavior complex. The velocity distribution of exponential-function driving has a high gradient, with the edge velocity significantly higher than the center velocity. This excites significant elastic and viscous stresses in viscoelastic fluids, resulting in a significant decrease in the average velocity generated by exponential-function driving in viscoelastic fluids.

The average velocity of logarithmic-function driving shows a unique "first-decreasing-then-increasing" trend as 0.2μm/s increases ($\bar{v}_{min} = 0.437\mu\text{m/s}$, $\mu_p = 0.002\text{Pa}\cdot\text{s}$; $\bar{v}_{max} = 0.474\mu\text{m/s}$, $\mu_p = 0.01\text{Pa}\cdot\text{s}$). This behavior stems from the nonlinear coupling between the gradient of the driving function and the shear-thinning of the fluid. In the low-$\mu_p$ range ($\mu_p < 0.002\text{Pa}\cdot\text{s}$), under the dominance of fluid elasticity, the gentle velocity gradient (gradual change of velocity from the center to the edge) of logarithmic driving cannot effectively excite the stretching stress field. At this time, the accumulation of elastic stress $\boldsymbol{T_e}$ is insufficient, resulting in a propulsion efficiency lower than that of exponential driving. In the medium-and high-$\mu_p$ range ($\mu_p > 0.002\text{Pa}\cdot\text{s}$), the shear-thinning effect of the LPTT model is significantly enhanced. The high shear rate in the edge region leads to a local decrease in viscosity, reducing energy dissipation. At the same time, the low shear rate of logarithmic driving in the central region maintains a relatively high-viscosity "pseudo-solid core"[47][48], forming a stable propelling force anchor point. Finally, the velocity recovery is achieved through the viscosity difference between the edge and the center.

The average velocity of sinusoidal driving is extremely insensitive to the change of $\mu_p$, with the average velocity variation $\Delta\bar{v} < 0.007\mu\text{m/s}$, always maintaining inefficient propulsion. Its periodic velocity fluctuations lead to the alternating generation of stretching and compression stress fields in

the flow field, causing energy dissipation: the periodic velocity changes induce the rapid relaxation of elastic stress $\boldsymbol{T_e}(\lambda\frac{\nabla}{\nabla t}\boldsymbol{T_{em}})$, generating an additional energy dissipation pathway and may also cause nonlinear resonance suppression. In addition, numerical errors or the marginal effects of nonlinear terms in the model may also have a certain impact on the results.

The results of this set of simulation experiments can guide the selection of robot driving modes. For instance, in a blood-like environment ($\mu_p \approx 0.003\text{Pa}\cdot\text{s}$), exponential driving is employed to maximize the utilization of elastic stress. In a mucus-like environment ($\mu_p \approx 0.008\text{Pa}\cdot\text{s}$), switch to logarithmic driving to optimize energy transfer through shear-thinning. Meanwhile, the relatively high robustness of the sinusoidal function can be well-exploited.

3.3 Research Results on $\lambda$ in Viscoelastic Fluids of the LPTT Constitutive Model

Next, with $\mu_p$ and $\varepsilon$ held constant at 0.001 $\text{Pa}\cdot\text{s}$ and 0.01 respectively, $\lambda$ is varied within the range of 0.01-0.1 s. (Figure 5) shows the influence of $\lambda$) on the average velocity $\bar{v}$ of the microrobot under three driving functions in viscoelastic fluids. The horizontal axis represents $\lambda$ (unit: s), and the vertical axis represents $\bar{v}$ (unit: $\mu\text{m/s}$). The results are as shown in (Figure 5).

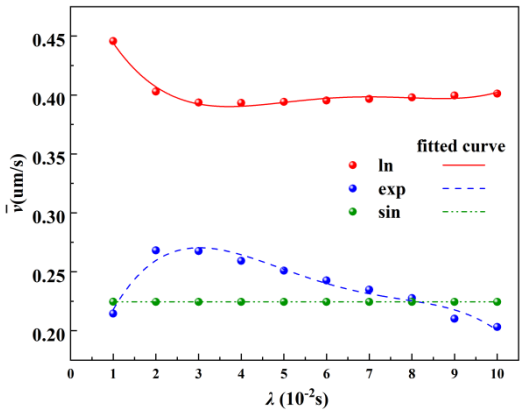


Figure 6: The results of $\bar{v}$ obtained from simulations where $\lambda$ varies in the range of 0.01-0.1 s in the viscoelastic fluid of the LPTT constitutive model, with $\mu_p$ and $\varepsilon$ kept constant at $0.001\text{Pa}\cdot\text{s}$ and 0.01 respectively, The blue (exp), red (ln), and green (sin) represent the results under three driving velocities respectively. The corresponding three curves are fitting curves.

As can be seen from the figure, under exponential-function driving, $\bar{v}$ rapidly rises from $0.215\mu\text{m/s}$ at $\lambda = 0.01\text{s}$ to a peak value of $0.268\,\mu\text{m/s}$ at $\lambda = 0.02\text{s}$, and then gradually decreases to $0.203\mu\text{m/s}$ at $\lambda = 0.1$ s. The experimental data is highly consistent with the dynamic process of elastic stress accumulation-relaxation of the LPTT model. When $\lambda < 0.02\text{s}$, the relaxation time of polymer chains is short, the elastic stress $\boldsymbol{T_e}$ relaxes rapidly, and the term $\lambda\frac{\nabla}{\nabla t}\boldsymbol{T_{em}}$ dominates, resulting in insufficient stress accumulation.

At this time, the high-gradient velocity distribution of exponential-function driving (the edge velocity is significantly higher than the center velocity) can partially excite the stretching stress, but is limited by the rapid dissipation during the relaxation process, resulting in low propulsion efficiency.$\lambda = 0.02$ s is the inflection point of the trend change. The increase in $\lambda$ delays the relaxation of elastic stress, allowing $\boldsymbol{T_e}$ to accumulate for a longer time in the flow field, forming a stronger stretching stress reaction force. At this time, the velocity gradient of exponential driving and the stress accumulation rate reach the best match, and the velocity reaches the peak value. After this point, the excessively long relaxation time leads to the excessive accumulation of elastic stress $\boldsymbol{T_e}$, causing local stress concentration (such as at the tail of the robot), generating a reverse resistance $\nabla\cdot\boldsymbol{T_e}$. Meanwhile, the stretching viscosity $\eta_e(\propto \mu_p\lambda)$of polymer chains in the LPTT model increases significantly, further suppressing the fluid flow, and ultimately leading to a decrease in velocity. It can be seen that in a low-$\lambda$ environment such as lymph fluid, exponential driving is adopted to rapidly excite elastic stress. Because the short relaxation time enables the elastic stress to quickly respond to the change in velocity gradient, thus generating an effective propelling force.

Under logarithmic function driving, $\bar{v}$ decreases from $0.446\mu m/s$ at $\lambda = 0.01s$ to a peak value of $0.394\mu m/s$ at $\lambda = 0.03s$, and then tends to be stable, showing an "L-like" curve with an overall "first-decreasing-then-stable" trend. In the initial decreasing stage when $\lambda$ ranges from 0.01s to 0.03s, the gentle velocity gradient of logarithmic driving (gradual change of velocity from the center to the edge) can partially utilize the elastic stress accumulation at low $\lambda$. However, as $\lambda$ increases, the relaxation time of polymer chains prolongs, and the local overload of elastic stress $\boldsymbol{T_e}$ (such as in the edge region) causes energy dissipation, resulting in a decrease in velocity. In the stable stage when $\lambda > 0.03s$, the shear-thinning effect of the LPTT model is significantly enhanced at high $\lambda$. The high shear rate in the edge region leads to a decrease in viscosity, offsetting the negative impact of elastic stress overload, and ultimately forming a dynamic equilibrium, with the velocity tending to be stable.

The fitting curve of the results under sinusoidal-function driving is nearly horizontal, indicating that it is extremely insensitive to the change of $\lambda$. $\bar{v}$ is always maintained between $0.224\mu m/s$ and $0.225\mu m/s$. This reflects the mismatch mechanism between periodic fluctuations and elastic relaxation. The periodic velocity changes of sinusoidal driving are much lower than the relaxation frequency of polymer chains $f_{relax} = 1/\lambda$, resulting in a phase lag in the response of elastic stress $\boldsymbol{T_e}$, and unable to form an effective accumulation of propelling force. Meanwhile, the periodic flow field disturbance induces the non-uniform distribution of elastic turbulence $\nabla \cdot \boldsymbol{T_e}$, further exacerbating energy dissipation, so that the efficiency of sinusoidal driving is always maintained at a low level.

Through simulation, the influence of $\lambda$ on the motion of microrobots is revealed, and its essence is the dynamic balance of elastic stress accumulation and relaxation. This discovery provides key parameter data for the optimization of driving strategies.

### 3.3 Research Results on $\varepsilon$ in Viscoelastic Fluids of the LPTT Constitutive Model

Finally, a simulation study was conducted on the influence of the change of the third parameter $\varepsilon$ in the LPTT constitutive equation on the robot's velocity. With $\mu_p$ and $\lambda$ kept constant at $0.001Pa \cdot s$ and 0.01s respectively, $\varepsilon$ was varied in the range of 0.01-0.1.

It is easy to see that the fitting curves of the average velocities of the robot under the three driving methods are all approximately horizontal lines. Under exponential driving, $\bar{v}$ slightly decreases from $0.21456\ \mu m/s$ at $\varepsilon = 0.01$ to $0.21411\ \mu m/s$ at $\varepsilon = 0.1$, with a change amplitude of only $0.00045\mu m/s$. Under logarithmic driving, $\bar{v}$ slightly increases from $0.44573\mu m/s$ at the initial stage to $0.44586\mu m/s$, with almost no change. Under sinusoidal driving, the fitting curve is almost a perfect horizontal line, indicating that the change of $\varepsilon$ within the experimental range has no observable effect on its propulsion efficiency.

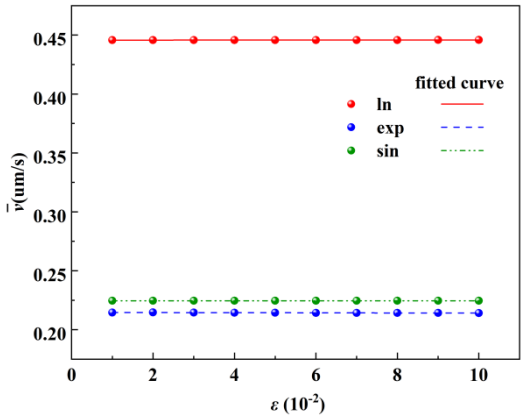


Figure 7 The results of $\varepsilon$ obtained from simulations where $\bar{v}$ varies in the range of 0.01-0.1. in the viscoelastic fluid of the LPTT constitutive model, with $\mu_p$ and $\lambda$ kept constant at $0.001Pa \cdot s$ and 0.01s respectively, The blue (exp), red (ln), and green (sin) represent the results under three driving velocities respectively. The corresponding three curves are fitting curves.

A further analysis of the experimental results reveals the following reasons. First, the coupling effect between the variation range of $\varepsilon$ (0.01-0.1) in the experiment and other model parameters is weak. For example, when $\mu_p = 0.001\text{Pa}\cdot\text{s}$ and $\lambda = 0.01\text{s}$, the magnitude of the coefficient $\frac{\lambda}{\mu_p}\varepsilon$ of the nonlinear term is $10\varepsilon$. For $\varepsilon = 0.1$, this coefficient is 1, which theoretically should significantly affect the model response. Second, the value of $\text{tr}(\boldsymbol{T_{em}})$ in the actual simulation may be low, resulting in a small actual contribution of the nonlinear term, thus weakening the influence of $\varepsilon$. Meanwhile, the two-dimensional flow field adopted in the experiment is mainly shear-flow, and the stretching component (such as the acceleration-deceleration zone along the flow direction) is weak. Since ε mainly regulates the stretching viscosity $\eta_e$, its effect is masked in the shear-dominated flow field, leading to insufficient data sensitivity. Considering the spatial characteristics of the driving function, during exponential and logarithmic driving, the velocity gradient mainly excites the shear stress $\boldsymbol{\tau}$, and $\varepsilon$ has little direct influence on the shear viscosity. During sinusoidal driving, although the periodic fluctuation may induce stretching flow, it is limited by the low $\lambda$ (0.01s), and the elastic stress relaxes rapidly, so the stretching viscosity effect is not fully accumulated.

## 4. Conclusion

This research systematically explores the motion dynamics of capsule-shaped microrobots in Newtonian and viscoelastic fluids under complex boundary conditions, with a focus on the coupling effect between rheological parameters and surface-driven propulsion strategies. Through the integration of theoretical modeling, numerical simulation, and parameter sensitivity analysis, the following key conclusions are drawn:

First, in Newtonian fluids, the velocity of microrobots is significantly affected by the proximity of sinusoidal-waveform boundaries, which stems from the interaction of boundary layers. The exponential-type surface-driven velocity distribution exhibits excellent propulsion efficiency, which is attributed to the stable hydrodynamic thrust generated by its high-velocity gradient at the edge. In contrast, the periodic fluctuations of the sinusoidal velocity distribution reduce the propulsion stability. These findings highlight the crucial role of boundary-layer dynamics and surface velocity distribution in the optimization of low-Reynolds-number motion.

The behavior of viscoelastic fluids and parameter coupling: Analysis of viscoelastic fluids based on the LPTT constitutive model reveals the nonlinear interaction between rheological parameters and propulsion efficiency:

Polymer viscosity $\mu_p$: The critical threshold($\mu_p = 0.005\text{Pa}\cdot\text{s}$) dominates the transition from elasticity-dominated to viscosity-dominated. In low-$\mu_p$ fluids (such as blood), exponential driving can maximize the utilization of elastic stress; while in high-$\mu_p$ fluids (such as mucus), logarithmic driving optimizes energy transfer through the shear-thinning effect.

Relaxation time $\lambda$: A short-$\lambda$ environment (such as lymph fluid) is conducive to rapid stress response, while an excessively long-λ causes energy dissipation through local stress concentration.

Elongation rate parameter ε: Within the tested range ($0.01 \le \varepsilon \le 0.1$), the influence of $\varepsilon$ on the shear-dominated flow field is negligible.

The research results provide practical guidance for the design of microrobots in clinical scenarios. In targeted drug-delivery applications, exponential driving is suitable for the blood environment, while logarithmic driving is suitable for mucus-rich regions. In other applications, for example, through $\lambda$-sensitive adaptive propulsion control, the penetration efficiency in fibrin-rich flow fields can be improved to achieve thrombus navigation.

In summary, this research establishes a basic framework for the motion of microrobots in complex rheological environments. Through the deep integration of data and theory, it emphasizes the core roles of surface driving, fluid-solid coupling, and multi-parameter synergy. By addressing theoretical and application challenges, it reveals the nonlinear influence of $\mu_p$, $\lambda$ and $\varepsilon$ on the motion of microrobots. The research achievements lay the foundation for a new generation of medical

microrobots, enabling them to achieve precise navigation in physiologically realistic environments and providing quantitative basis and innovative ideas for the design of driving strategies in clinical translation.

## References

[1] H. Liu, Q. Guo, W. Wang, T. Yu, Z. Yuan, Z. Ge, and W. Yang, "A review of magnetically driven swimming microrobots: Material selection, structure design, control method, and applications," REVIEWS ON ADVANCED MATERIALS SCIENCE 62(1), 20230119 (2023).

[2] F. Wei, T. Zhong, Z. Zhan, and L. Yao, "Self-assembled Micro-nanorobots: From Assembly Mechanisms to Applications," ChemNanoMat 7(3), 238–252 (2021).

[3] M. Luo, Y. Feng, T. Wang, and J. Guan, "Micro-/Nanorobots at Work in Active Drug Delivery," Adv Funct Materials 28(25), 1706100 (2018).

[4] J. Li, E.S. Barjuei, G. Ciuti, Y. Hao, P. Zhang, A. Menciassi, Q. Huang, and P. Dario, "Magnetically-driven medical robots: An analytical magnetic model for endoscopic capsules design," Journal of Magnetism and Magnetic Materials 452, 278–287 (2018).

[5] M. Xie, W. Zhang, C. Fan, C. Wu, Q. Feng, J. Wu, Y. Li, R. Gao, Z. Li, Q. Wang, Y. Cheng, and B. He, "Bioinspired Soft Microrobots with Precise Magneto-Collective Control for Microvascular Thrombolysis," Advanced Materials 32(26), 2000366 (2020).

[6] M. Wan, Q. Wang, R. Wang, R. Wu, T. Li, D. Fang, Y. Huang, Y. Yu, L. Fang, X. Wang, Y. Zhang, Z. Miao, B. Zhao, F. Wang, C. Mao, Q. Jiang, X. Xu, and D. Shi, "Platelet-derived porous nanomotor for thrombus therapy," Sci. Adv. 6(22), eaaz9014 (2020).

[7] Y. Zhang, L. Zhang, L. Yang, C.I. Vong, K.F. Chan, W.K.K. Wu, T.N.Y. Kwong, N.W.S. Lo, M. Ip, S.H. Wong, J.J.Y. Sung, P.W.Y. Chiu, and L. Zhang, "Real-time tracking of fluorescent magnetic spore–based microrobots for remote detection of C. diff toxins," Sci. Adv. 5(1), eaau9650 (2019).

[8] S. Varchanis, C.C. Hopkins, A.Q. Shen, J. Tsamopoulos, and S.J. Haward, "Asymmetric flows of complex fluids past confined cylinders: A comprehensive numerical study with experimental validation," Physics of Fluids 32(5), 053103 (2020).

[9] I.C. Yasa, H. Ceylan, U. Bozuyuk, A.-M. Wild, and M. Sitti, "Elucidating the interaction dynamics between microswimmer body and immune system for medical microrobots," Sci. Robot. 5(43), eaaz3867 (2020).

[10] B.E.-F. De Ávila, P. Angsantikul, J. Li, M. Angel Lopez-Ramirez, D.E. Ramírez-Herrera, S. Thamphiwatana, C. Chen, J. Delezuk, R. Samakapiruk, V. Ramez, M. Obonyo, L. Zhang, and J. Wang, "Micromotor-enabled active drug delivery for in vivo treatment of stomach infection," Nat Commun 8(1), 272 (2017).

[11] R. Mundaca-Uribe, B. Esteban-Fernández De Ávila, M. Holay, P. Lekshmy Venugopalan, B. Nguyen, J. Zhou, A. Abbas, R.H. Fang, L. Zhang, and J. Wang, "Zinc Microrocket Pills: Fabrication and Characterization toward Active Oral Delivery," Adv Healthcare Materials 9(18), 2000900 (2020).

[12] Z. Wu, J. Troll, H.-H. Jeong, Q. Wei, M. Stang, F. Ziemssen, Z. Wang, M. Dong, S. Schnichels, T. Qiu, and P. Fischer, "A swarm of slippery micropropellers penetrates the vitreous body of the eye," Sci. Adv. 4(11), eaat4388 (2018).

[13] J. Choi, J. Hwang, J. Kim, and H. Choi, "Recent Progress in Magnetically Actuated Microrobots for Targeted Delivery of Therapeutic Agents," Adv Healthcare Materials 10(6), 2001596 (2021).

[14] Z. Wu, Y. Chen, D. Mukasa, O.S. Pak, and W. Gao, "Medical micro/nanorobots in complex media," Chem. Soc. Rev. 49(22), 8088–8112 (2020).

[15] D. Chen, J. Li, H. Chen, L. Zhang, H. Zhang, and Y. Ma, "Electroosmotic Flow Behavior of Viscoelastic LPTT Fluid in a Microchannel," Micromachines 10(12), 881 (2019).

[16] S.E. Spagnolie, editor , Complex Fluids in Biological Systems: Experiment, Theory, and Computation (Springer New York, New York, NY, 2015).

[17] F. Pinto, and M. Meo, "Design and Manufacturing of a Novel Shear Thickening Fluid Composite (STFC) with Enhanced out-of-Plane Properties and Damage Suppression," Appl Compos Mater 24(3), 643–660 (2017).

[18] L.A. Green, “The swimming performance of microrobots in tight spaces,” Scilight 2023(35), 351101 (2023).

[19] E.M. Jolley, R.A. Palmer, and F.T. Smith, “Particle movement in a boundary layer,” J Eng Math 128(1), 6 (2021).

[20] K. Kim, J. Guo, Z.X. Liang, F.Q. Zhu, and D.L. Fan, “Man-made rotary nanomotors: a review of recent developments,” Nanoscale 8(20), 10471–10490 (2016).

[21] S. Jafari Kang, S. Sur, J.P. Rothstein, and H. Masoud, “Forward, reverse, and no motion of Marangoni surfers under confinement,” Phys. Rev. Fluids 5(8), 084004 (2020).

[22] W. Waheed, E. Abu-Nada, and A. Alazzam, “Microparticle motion under dielectrophoresis: immersed boundary—Lattice Boltzmann-based multiphase model and experiments,” Comp. Part. Mech. 11(3), 1281–1299 (2024).

[23] Z. Ouyang, C. Liu, T. Qi, J. Lin, and X. Ku, “Locomotion of a micro-swimmer towing load through shear-dependent non-Newtonian fluids,” Physics of Fluids 35(1), 013334 (2023).

[24] C.-T. Liao, A. Lemus, A. Gürbüz, A.C.H. Tsang, O.S. Pak, and A. Daddi-Moussa-Ider, “Propulsion of a three-sphere microrobot in a porous medium,” Phys. Rev. E 109(6), 065106 (2024).

[25] A. Baruah, On The Gaussian-Core Vortex Lattice Model for The Analysis of Wind Farm Flow Dynamics, Doctor of Philosophy in Mechanical Engineering-Engineering Mechanics, Michigan Technological University, 2023.

[26] Z.-G. Feng, and E.E. Michaelides, “The immersed boundary-lattice Boltzmann method for solving fluid–particles interaction problems,” Journal of Computational Physics 195(2), 602–628 (2004).

[27] A. Del Buono, G. Bernardini, A. Tassin, and A. Iafrati, “Water entry and exit of 2D and axisymmetric bodies,” Journal of Fluids and Structures 103, 103269 (2021).

[28] R.W. Anderson, N.S. Elliott, and R.B. Pember, “An arbitrary Lagrangian–Eulerian method with adaptive mesh refinement for the solution of the Euler equations,” Journal of Computational Physics 199(2), 598–617 (2004).

[29] Q. Cao, and L. Nastac, “Mathematical Investigation of Fluid Flow, Mass Transfer, and Slag-steel Interfacial Behavior in Gas-stirred Ladles,” Metall Mater Trans B 49(3), 1388–1404 (2018).

[30] A. Aghakhani, A. Pena-Francesch, U. Bozuyuk, H. Cetin, P. Wrede, and M. Sitti, “High shear rate propulsion of acoustic microrobots in complex biological fluids,” Sci. Adv. 8(10), eabm5126 (2022).

[31] J. Chen, H. Hu, and Y. Wang, “MAGNETIC-DRIVEN SWIMMING MICROROBOTS,” in Proceedings of the 14th International Workshop on Structural Health Monitoring, (Destech Publications, Inc., 2023).

[32] Y. Murthy, and R. Banavar, “A Lagrangian Model to Predict Microscallop Motion in non Newtonian Fluids,” in 2019 International Conference on Manipulation, Automation and Robotics at Small Scales (MARSS), (IEEE, Helsinki, Finland, 2019), pp. 1–6.

[33] “Viscoelastic Flow Dynamics from Theory to,” (n.d.).

[34] Alaa Sharhan and Alaa H. Al-Muslimawi, “Numerical Study of Shear and Extensional Inelastic Contraction Flows,” CFDL 15(8), 107–121 (2023).

[35] C. Sasakawa, editor , Molecular Mechanisms of Bacterial Infection via the Gut (Springer Berlin Heidelberg, Berlin, Heidelberg, 2009).

[36] S.A. Lin, and N. Barker, “Gastrointestinal stem cells in self-renewal and cancer,” J Gastroenterol 46(9), 1039–1055 (2011).

[37] H. Ullah, D. Lu, A. Majeed Siddiqui, K. Maqbool, and S. Iqbal, “Fluid model using recursive approach: Application to permeable slit with uniform reabsorption and velocity slip,” Results in Physics 25, 104196 (2021).

[38] Y. Mu, N. Li, L. Hang, G. Zhao, J. Gao, and Z. Niu, “Investigation of the Rheological Behaviors of Polymeric Materials in the Film Casting Process through Multiscale Modeling and Simulation Method,” Macro Theory & Simulations 28(3), 1900001 (2019).

[39] L.L. Ferrás, M.L. Morgado, M. Rebelo, G.H. McKinley, and A.M. Afonso, “A generalised Phan–Thien—Tanner model,” Journal of Non-Newtonian Fluid Mechanics 269, 88–99 (2019).

[40] A.B.J.D. Silva, Estudo da Estabilidade de Escoamento de Fluido Não Newtoniano Modelado pelo LPTT, Mestrado em Ciências de Computação e Matemática Computacional, Universidade de São Paulo, 2022.

[41] W. Gao, K.M. Manesh, J. Hua, S. Sattayasamitsathit, and J. Wang, “Hybrid Nanomotor: A Catalytically/Magnetically Powered Adaptive Nanowire Swimmer,” Small 7(14), 2047–2051 (2011).

[42] B. Straughan, “Effect of anisotropy and boundary conditions on Darcy and Brinkman porous penetrative convection,” Environ Fluid Mech 22(6), 1233–1252 (2022).

[43] “Review on the Latest Research Progress of Micro-Nano Robots,” (n.d.).

[44] B. Wang, K. Kostarelos, B.J. Nelson, and L. Zhang, “Trends in Micro-/Nanorobotics: Materials Development, Actuation, Localization, and System Integration for Biomedical Applications,” Advanced Materials 33(4), 2002047 (2021).

[45] C. Datt, L. Zhu, G.J. Elfring, and O.S. Pak, “Squirming through shear-thinning fluids,” J. Fluid Mech. 784, R1 (2015).

[46] C. Lang, S. Adami, and N.A. Adams, “Viscoelastic vapor bubble collapse near solid walls and corresponding shock wave formation,” Physics of Fluids 36(1), 013110 (2024).

[47] Y. Ren, K.S. Koh, and Y. Zhang, “Synthesis of Functional Materials by Non-Newtonian Microfluidic Multiphase System,” in Advances in Microfluidics-New Applications in Biology, Energy, and Materials Sciences, edited by X.-Y. Yu, (InTech, 2016).

[48] M. Trejo-Cáceres, M.C. Sánchez, and J.E. Martín-Alfonso, “Impact of acetylation process of kraft lignin in development of environment-friendly semisolid lubricants,” International Journal of Biological Macromolecules 227, 673–684 (2023).

[49] M. Dessard, J.-B. Manneville, and J.-F. Berret, “Cytoplasmic Viscosity is a Potential Biomarker for Metastatic Breast Cancer Cells,” (n.d.).

[50] J.E. Moore, and C.D. Bertram, “Lymphatic System Flows,” Annu. Rev. Fluid Mech. 50(1), 459–482 (2018).